# Chemistry and Interfacial Structure Promoting Quasi-van der Waals Epitaxial-Growth of $WS_2$ Nanosheets on Sapphire for Prospective Application in Field-Effect Transistors

Supriyo Majumder[1], Nitin Shinde[2], John Cavin[3], Chen Chen[4], Arka Bikash Dey[5], K. V. L. V. Narayanachari[1], Jiaqi Zhang[1], David Garcia-Wetten[1], Oswaldo Dieguez[2], Simon Hettler[6,7], Assael Cohen,[2] Denis T. Keane[1], Raul Arenal[6,7,8], James M. Rondinelli[1], Ariel Ismach[2], Michael J. Bedzyk[1,9*]

[1]Department of Materials Science and Engineering, Northwestern University, Evanston, Illinois 60208, United States.

[2]Department of Materials Science and Engineering, Tel Aviv University, Ramat Aviv, Tel Aviv, 6997801, Israel.

[3]Department of Mechanical Engineering and Material Science, Washington University in St. Louis, St. Louis, Missouri 63130, United States.

[4]2D Crystal Consortium - Materials Innovation Platform, Materials Research Institute, The Pennsylvania State University, University Park, PA 16802, United States.

[5]Deutsches Elektronen-Synchrotron DESY, Hamburg 22607, Germany.

[6]Laboratorio de Microscopías Avanzadas (LMA), Universidad de Zaragoza, 50018 Zaragoza, Spain.

[7]Instituto de Nanociencia y Materiales de Aragón (INMA), CSIC−Universidad de Zaragoza, 50009 Zaragoza, Spain.

[8]ARAID Foundation, 50018 Zaragoza, Spain.

[9]Department of Physics and Astronomy, Northwestern University, Evanston, Illinois 60208, United States.

*bedzyk@northwestern.edu

**ABSTRACT:**

How do chemical and structural modifications to the supporting crystal surface affect the subsequent van der Waals (vdW) or quasi(Q)-vdW epitaxial growth of 2D nanocrystals? Developing an atomic-scale picture of such an interfacial system is crucial for understanding its impact on the physical and chemical properties of the supported 2D materials. The elucidation of the interfacial structure and chemistry needed to promote the Q-vdW epitaxial growth of 2D tungsten disulfide ($WS_2$) nanocrystals contributes to the growth mechanism understanding, thus pushing forward the integration of such atomically thin semiconductors toward real field-effect transistor applications. In addition to an atomic-force microscopy top view, we showcase a combination of X-ray techniques for a top-to-bottom investigation of the complexities of the buried interface structures. This approach uses X-ray photoelectron spectroscopy, X-ray standing wave excited X-ray fluorescence, and crystal truncation rod scattering to produce a highly resolved chemical-state-specific 3D atomic map for the extended interface structure of $WS_2/\alpha\text{-}Al_2O_3(001)$. Employing these detailed analysis methods, along with density functional theory to further refine the picoscale structure, we demonstrate how two different types of interface engineering during the pre-growth stage lead to significant differences in the chemical and structural modifications to the terminal surface of c-face sapphire, which in turn leads to substantial differences in sub-monolayer growth of supported $WS_2$ 2D nanocrystals in terms of lateral domain sizes, epitaxial registry, vdW gaps, and stability.

**KEYWORDS:** two-dimensional material, transition metal dichalcogenide, quasi-van der Waals epitaxy, interface engineering, non-destructive depth profiling, X-ray standing wave, crystal truncation rod scattering, interface structure

## INTRODUCTION:

Atomically thin, two-dimensional (2D) materials exhibit numerous functional properties dictated by their unique intralayer atomic arrangements that typically differ from their three-dimensional counterparts. One of the most striking examples is graphene, an extensively studied 2D system in which a superconducting state is achieved by introducing a specific angular twist between its interlayers.[1] Such a delicate manipulation in structure has become possible due to the weak van der Waals (vdW) interaction between the individual layers in 2D systems. Due to having an exceptional surface-to-volume ratio, the interface of the 2D crystal and substrate critically impacts the functional properties. The sharp discontinuity of a crystal at the terminal surface from its periodic lattice is expected to modify the local electronic properties. For example, the reconstructed interface in the epitaxial graphene (EG)/SiC (001) system significantly affects the carrier doping, band gap, and transport behaviors of the EG.[2] In 2D materials and heterostructure systems, the interfacial electronic states can have a delocalized nature and cross the Fermi level, resulting in a metallic pathway that directly impacts the charge transport.[3] Tungsten diselenide ($WSe_2$), a transition metal dichalcogenide (TMD) 2D system, is reported to exhibit drastic alteration in band structure near the Fermi level when the interface is changed from $WSe_2$/EG/SiC(001) to $WSe_2$/Se-terminated GaAs(111)B.[4] Different charge redistributions induced by these two interfaces also lead to n- and p-type carrier doping in the monolayer (ML) $WSe_2$/EG/SiC(001) and $WSe_2$/Se-terminated GaAs(111)B, respectively.[4]

Regardless of several fascinating properties, the zero-bandgap character of graphene leads to high leakage current and power dissipation issues, which hinders its use in numerous electronic applications including field-effect transistor (FET) devices.[5] In contrast, 2D TMDs possess tuneable bandgaps, including indirect to direct bandgap crossovers, valley-selective optical excitations, photo-current switching, and controllable surface mobilities favorable for various flexible nano-electronic applications.[6-8] In the TMD family of materials, tungsten disulfide ($WS_2$) is one of the promising candidates with intriguing properties applicable to FETs,[9] memristors,[2] photodetectors,[10] and light-emitting devices.[11] The recent discovery of light-excited photo-strictive behavior and n- to p-type conversion attributed to strong multimodal coupling in opto-electrical-mechanical properties drives the ML $WS_2$ to be a prime focus for fundamental and technological reasons.[12] Besides, a designed superstructure of $WS_2$ has been reported to exhibit efficient performance for hydrogen evolution reactions at industrial-level current densities.[13] Also, in ML $WS_2$ systems, as with other 2D materials, different substrate terminations are observed to have significant bearings on their electronic and optical properties.[14, 15]

One of the basic requirements for successfully integrating any 2D functional materials into existing device technologies (e.g. FET devices) is the ability to grow them in a desired fashion (structure, chemical composition, number of layers, morphology, etc.). In current state-of-the-art technology, epitaxial growth is the most reliable path for providing accurate control at the atomic scale of thin films used as building blocks in many device fabrication industries. For 2D TMDs, the foremost difference with conventional epitaxial thin films is the weaker Q-vdW interactions between the 2D nanocrystal and the supporting single crystal. Single crystal-supported epitaxial growth of $WS_2$ is the most effective way to reduce misaligned domains and, hence, is beneficial for making device-grade samples. The hexagonal c-face sapphire ($\alpha$-$Al_2O_3$(001)) surface is a popular choice for epitaxial growth of hexagonal $WS_2$ crystals because of their in-plane crystallographic compatibility with $3\times a_{WS2} \sim 2\times a_{Al2O3}$ or $5\times a_{WS2} \sim 2\sqrt{3}\times a_{Al2O3}$ domain epitaxies where, $a_{WS2} = 3.191$ Å and $a_{Al2O3} = 4.754$ Å.[16, 17] Previous work has demonstrated that the sticking coefficients for the TMD precursors on the $Al_2O_3$ surface are greater than other substrates, including EG, CVD graphene, and amorphous boron nitride, leading to larger 2D domains through surface diffusion of adsorbed species during lateral growth.[18] As domain boundaries in ML TMDs could reduce electronic performance, large unidirectional 2D single-crystal TMD domains are desirable for device applications.

There are a variety of different growth recipes that should result in different unexplored interface structures between the over-layer $WS_2$ nanocrystals and under-laying $\alpha$-$Al_2O_3$(001) single crystalline substrate.[17, 19] Despite earlier research endeavors, several striking and not yet understood differences in the literature regarding the 2D TMD growth on $\alpha$-$Al_2O_3$(001) need to be investigated comprehensively. In the present work, we will compare two cases that primarily differ in their engineering of the top atomic layers of the supporting surface. One is terminated with a $WO_3$ layer (W incorporation) and the other with an AlS (S incorporation) layer.

Herein, we show how the chemical and structural modifications of the supporting surface of sub-ML $WS_2$/ $\alpha$-$Al_2O_3$(001), formed at the early stage of the metal-organic chemical vapor deposition (MOCVD) process, intimately influence the subsequent growth of the 2D $WS_2$ nanocrystals. We use X-ray scattering and spectroscopy to reveal the atomic-scale, element-specific extended interface structures of W or S incorporations into the $\alpha$-$Al_2O_3$(001) surface terminating layer, the vdW gap (couple of *Å*-spacing between substrate surface termination atomic-layer and bottom atomic-layer of the 2D crystal), and the supported $WS_2$ 2D epi-layer. Our methodology features relatively non-destructive X-ray techniques, namely X-ray photoelectron spectroscopy (XPS) to identify the chemical states of the interfacial species, grazing incidence X-ray diffraction (GIXRD)[2015] to find the epitaxial orientation of the 2D crystal lattice with respect to the substrate, X-ray standing wave excited fluorescence (XSW-XRF)[21-23] to locate W or S atomic positions relative to the substrate lattice, and crystal truncation rod (CTR)[24-26] scattering to produce a 3D electron density map of the extended interfacial structure. We also use atomic force microscopy (AFM) as a local probe for multilength scale surface topography and cross-sectional scanning transmission electron microscopy (STEM) for a side view of the interface structure. We demonstrate how the two different MOCVD recipes lead to changes in chemical and structural terminations of the supporting substrate surface. We then link these foundational differences to significant differences we find in the supported 2D crystals in terms of their lateral 2D crystal sizes, epitaxial registry, and vdW gaps. Our density functional theory (DFT) calculations confirm the structural findings and provide information for the (X-ray invisible) H atomic positions at the substrate terminal surface and adhesion energy associated with vdW bonding at the interface. The developed atomic-scale characterization methodology will apply to supported 2D crystals in general and should be beneficial for optimizing device grade preparation of 2D $WS_2$.

## EXPERIMENTAL:

### Synthesis

**$WS_2$/$\alpha$-$Al_2O_3$(001) sample T** was grown at the 2D Materials lab at Tel Aviv University. The $\alpha$-$Al_2O_3$(001) substrate was pre-annealed for *10 h* at *1050$^o$ C* in air. The synthesis of $WS_2$ was carried out on c-plane sapphire (2” diameter) substrate using a 3” hot wall customized MOCVD system (CVD Equipment Corporation, model Easy Tube 2000), equipped with four separate bubblers for all the precursors.[27] Prior to loading the substrates in MOCVD, they were cleaned by ultrasonication in acetone and IPA (each for *10* min), followed by blow drying with a nitrogen gun. Pre-annealing: Before the growth process started, the $Al_2O_3$(001) substrate was in-situ annealed for *30 min* under *50 mTorr* $O_2$ pressure (*100 sccm* flow) at *850 $^o$ C* inside the MOCVD furnace. Then, the oxygen flow was stopped, and the furnace was maintained at *850° C* for another *25 min*. Metal seeding step: Tungsten hexacarbonyl ($W(CO)_6$ - Strem Chemicals Inc., *99.9%*) precursor was flown (no S source) at a rate of $\sim 3.28 \times 10^{-7}$ *mol/min* with Ar as background gas for *5 min*. Growth: The $W(CO)_6$ flow was reduced to $\sim 1.31 \times 10^{-8}$ *mol/min* and Di-tert-butyl sulfide (DTBS-Sigma Aldrich, *97%*) precursor was introduced at a rate $\sim 3.25 \times 10^{-4}$ *mol/min* with *5 mmol/min* $H_2O$, *25 sccm* of $H_2$, and *500 sccm* of Ar as background gas. The furnace temperature was maintained constant at *850°* C throughout pre-annealing, metal seeding, and growth steps. Lateral domain formation of $WS_2$ was carried out by 15 min growth using all precursors ($W(CO)_6$, DTBS, $H_2O$, $H_2$). This gives rise to a sub-ML $WS_2$/$Al_2O_3$(001) sample, labeled as sample – T. The $WS_2$ growth rate for sample T is estimated to be *~0.035* ML*/min*. To investigate the interface structure between the $WS_2$ and $Al_2O_3$(001) crystals, a separate sample was taken out from the MOCVD furnace after $Al_2O_3$(001) interacted with

$W(CO)_6$ in the metal seeding step, before going to the growth step. This sample is labeled as $WO_3/Al_2O_3(001)$ (in the results and discussion section, we have concluded that the metal seeding step forms a $WO_3$-seeded interface on $Al_2O_3(001)$).

**$WS_2/\alpha$-$Al_2O_3(001)$ sample P** was grown at the 2D Crystal Consortium Materials Innovation Platform located at Pennsylvania State University. As received, c-plane sapphire (2” diameter) was used for the growths without additional pretreatment. Pre-annealing: Before growth, the $Al_2O_3(001)$ substrate was in-situ annealed for *10 min* at *850$^o$ C* in $H_2$. The growth of sub-ML $WS_2$ on 2” diameter c-plane sapphire was carried out in a MOCVD system equipped with a cold-wall horizontal reactor with an inductively heated graphite susceptor with gas-foil wafer rotation (Instrument DOI: 10.60551/znh3-mj13). Tungsten hexacarbonyl ($W(CO)_6$) was used as the metal precursor, while hydrogen sulfide ($H_2S$) was the chalcogen source with $H_2$ as the carrier gas. The $W(CO)_6$ powder was maintained at *25 °C* and *400 Torr* in a stainless-steel bubbler. The synthesis of $WS_2$ is based on a multi-step process, consisting of nucleation, ripening, and lateral growth steps, which was described elsewhere.[19] In general, the $WS_2$ was nucleated for *30 sec* at *850$^o$ C*, then ripened for *20 min* at *850$^o$ C* and *10 min* at *1000$^o$ C*, and then $WS_2$ was grown laterally for a shorter time, *10 min* at *1000° C*, which gives rise to a sub-ML $WS_2$ sample. During nucleation the flow rates of the $W(CO)_6$ and $H_2S$ precursors were ~ $1.3 \times 10^{-4}$ and *400 sccm*, respectively. In the ripening step, $W(CO)_6$ flow was turned off, keeping the $H_2S$ flow rate constant. The lateral growth was carried out with the $W(CO)_6$ flow rate at $6.4 \times 10^{-5}$ sccm, and the chalcogen flow rate was set at *400* sccm, while the reactor pressure was kept at *50 Torr*. After growth, the substrate was cooled in $H_2S$ to *300* °C to inhibit the decomposition of the deposited $WS_2$ films. This sample was labeled as $WS_2/Al_2O_3(001)$ - P. The growth rate for sample P was ~*0.065* ML*/min*. The sample’s detailed growth recipe and all initial characterization data are available at: https://m4-2dcc.vmhost.psu.edu/list/data/100.

## Characterization

**AFM:** The surface topographic characterizations shown in the Figs.1(a, b) were performed using AFM measurements in tapping mode at the institutes where samples T and P were grown. A UHV Omicron VT-SPM in the X-ray Interface Science Lab at Northwestern University was used in contact mode for the high-resolution AFM image shown in Fig. 1(c). The UHV chamber is isolated from external vibrations, and the SPM has built-in magnetic levitation. The sample was annealed at *300° C* for *30 min* in the Omicron UHV chamber before the AFM imaging.

**In-House X-ray Studies:** In-house X-ray diffraction measurements (discussed in SI) used a Rigaku SmartLab instrument with a *9 kW* Cu anode, Ge(220) 2-bounce monochromator, and a 5-circle diffractometer. The incident X-ray flux of wavelength $\lambda = 1.541$ Å on the sample was $3.3 \times 10^7$ photons per second. Surface composition and coverage were determined using XPS and XRF measurements. XPS used a Thermo Scientific ESCALAB 250 Xi instrument with an Al $K\alpha$ monochromated source, *500 μm* X-ray beam diameter, *50 eV* analyzer pass energy, and an electron flood gun. XRF measurements were performed using a Rigaku *18 kW* Mo anode X-ray source, multilayer monochromator, Huber 2-circle diffractometer, and Vortex silicon drift diode X-ray fluorescence detector with deadtime correction. The absolute coverage of W was determined by comparison to an RBS-calibrated standard sample. The XSW-XRF of sample P also used this in-house setup.

**Synchrotron XSW-XRF:** The XSW-XRF measurements (discussed in SI) of $WO_3/Al_2O_3(001)$ and sample T used the Advanced Photon Source (APS) 5ID-C DuPont-Northwestern-Dow Collaborative Access Team (DND-CAT) undulator station.[28] For W $L\alpha$ and S $K\alpha$ XSW-XRF measurements, we used two incident photon energies $E_\gamma = 15.00\ keV$ and *8.00 keV* selected by Si(111) and Si(220) monochromators respectively and further conditioned with a Si(220) post-monochromator channel-cut crystal (See Fig. S6.). The incident beam size was set to *0.1 mm* high by *0.2 mm* wide. The XSW-XRF measurements used a Huber Kappa 5-circle diffractometer and a Vortex silicon drift diode (SDD) XRF detector.

**Synchrotron CTR:** Specular and off-specular CTR measurements (discussed in SI) of $WO_3/Al_2O_3(001)$ and sample T used the P08 High Resolution Diffraction beamline,[29] which resides at the PETRA III

Deutsches Elektronen-Synchrotron (DESY) facility. The incident X-ray beam of energy $E_\gamma \sim 18\ keV$ from the undulator of P08 was conditioned by a Si(111) high-heat load monochromator, and Si(511) large offset monochromator, followed by compound refractive lenses and beam defining slits *0.1 mm*-high by *0.4 mm*-wide. The incident beam wavelength was calibrated by recording data for a standard $LaB_6$ sample, and the estimated value was $\lambda = 0.6897$ Å. CTR experiments used a KOHZU NZD-3 high-precision 6-circle diffractometer and Dectris Pilatus 100k pixel area detector. The details about the background subtractions and different corrections of CTR data can be found in Ref.[30]

## Theory

**DFT for $WO_3$ / $Al_2O_3$(001):** DFT calculations for the $WO_3/Al_2O_3$(001) structure used the Vienna Ab-initio Simulation Package (VASP) following the same approach as we did in Ref.[17], including resorting to the Perdew-Burke-Ernherzof (PBE) functional to describe the exchange-correlation effects. The O-terminated alumina slabs with a plane of mirror symmetry through their centers were built using DFT optimized unit cell of $Al_2O_3$ (a = *4.773 Å* and c = *13.008 Å*), containing alternating O layers (seven) and metal bilayers (six); H atoms were added as needed to allow each ion in its favored valence state. Using symmetric slabs allowed for exact calculations of the energy without having to add an electrostatic correction. The dimension of the slab supercell was set to $\sqrt{3}a \times 2a \times (c + 10$ Å), (here we considered *10 Å* of vacuum between periodic copies of the slabs). We then introduced different amounts of W substitutions in the outermost metal bilayers of these slabs with site fractions *12.5, 25, 37.5,* and *50 %* testing for all possible inequivalent arrangements of W incorporations in the chosen supercell.

**DFT for $WS_2$ / $Al_2O_3$(001) sample P:** DFT calculations for sample P used VASP.[31, 32] All calculations were carried out with the PBE formalism of the generalized gradient approximation.[33] The Monkhorst-Pack method was used to generate the *k*-point meshes.[34] The number of *k*-point divisions along direction *i*, $N_i$, was chosen such that $N_i \times a_i \approx 25$ Å for geometric optimization and $N_i \times a_i \approx 75$ Å for static calculations, with $a_i$ being the length of the lattice parameter in the *i* direction. The kinetic energy cutoff for the plane-wave basis was *500 eV*, and geometric optimization of the atomic positions was performed with a maximum force criterion of *0.01 eV/Å*. The lattice parameter of all supercell slabs was fixed to the relaxed bulk alumina structure, while atomic positions were allowed to relax. Each slab calculation had at least *10 Å* of vacuum spacing to minimize image interactions. The AlS slab ($Al_2O_3$+AlS) was constructed with 6 sub-layers of Al. The AlS slab was relaxed in the 2×2×1 supercell to allow for possible surface reconstruction. The AlS / $Al_2O_3$(001) slab calculation was done with a 2x2x1 supercell of AlS and two symmetric 3×3×1 supercells of $WS_2$. To produce a reference energy for adhesion energy, the $WS_2$ sheet had its atomic positions relaxed within a 3×3×1 supercell fixed to the in-plane lattice parameters of the 2×2×1 bulk relaxed $Al_2O_3$. The formula for the adhesion energy is given by $E_{adhesion} = \left( E_{AlS+WS_2} - E_{AlS} - 2E_{WS_2} \right) / 2A$ where $A$ is the in-plane area of the supercells.

## RESULTS:

Sub-ML $WS_2/\alpha\text{-}Al_2O_3$(001) samples, labeled T and P, were synthesized by two different MOCVD growth processes schematically depicted in Figs. 1(a, b) and described in the Methods Section. Both samples were grown on *0.5 mm* thick $Al_2O_3$(001) single crystal substrates with ~ $0.2^o$ miscut (Fig. S2(b, c)). Before $WS_2$ lateral growth with a gas mixture containing W and S precursors, the MOCVD process for sample T started with a high $W(CO)_6$ flux (no S flux) called the metal seeding step to an oxygen-terminated $Al_2O_3$(001) surface.[17] In contrast, the sample P growth started with a high $H_2S$ flux (very low $W(CO)_6$ flux) in the initial treatment step called nucleation on an Al-terminated $Al_2O_3$(001) surface.[19] AFM images of the grown surfaces, as presented in insets of Figs. 1(a, b), show equilateral triangles of $WS_2$ domains for both samples T and P. These 2D equilateral triangles have equal populations of bidirectional domains in both samples T and P (a bigger region AFM scan of sample T shows bidirectional domains as reported in Ref.[17]). Remarkably, the typical triangle lateral size for sample T of *8-10 µm* is much larger than the *40-50 nm* typical size for sample P. The growth rate for sample T was slower than that of sample P, as discussed in the Methods Section. However, it is not possible to compare the growth kinetics between two different MOCVD processes operating with different precursors and growth methods. One plausible reason for the larger 2D lateral domain growth is the lower nucleation site density in sample T than that of sample P, as observed in the AFM micrographs of the intermediate stage samples taken out of the MOCVD chamber before $WS_2$ lateral domain growth starts, presented in Refs.[17, 19]. Synthesis conditions, including temperature, chalcogen to metal precursor ratio, total precursor pressure, and flow rate, play a significant role in the nucleation density and hence on the lateral domain sizes of the gown 2D crystals. As reported in previous work about $WSe_2$ growth on a sapphire substrate, an increase in temperature and Se to W precursor ratio resulted in larger lateral 2D domains.[18] Keeping the temperature and Se to W precursor ratio fixed, an increase in total precursor pressure was found to decrease the nucleation density, leading to an increase in the lateral domain size.[18] Whereas, the lateral domain size decreases when the precursor flow rate increases with fixed growth temperature, precursor pressure, and Se to W precursor ratio at optimized values.[18] In the present work, we have used two different MOCVD synthesis approaches to engineer chemically and structurally different terminations of the $Al_2O_3(001)$ substrate for subsequent growth of sub-monolayer $WS_2$ crystals. During the $WS_2/Al_2O_3$ growth optimization, we tested different synthesis strategies but never succeeded in growing unidirectional epitaxial $WS_2$ crystals until either we used a W metal seeding approach, as used for sample T, or a very high S precursor flux to start with the nucleation, as used for the sample P. For example, as reported in previous work, without a W metal seeding, the grown $WS_2$ crystals show random in-plane orientations with the substrate crystal.[27] As the MOCVD processes for the $WS_2/Al_2O_3(001)$ samples T and P use different precursors, the growth parameters are not directly comparable to correlate how these two synthesis routes provide dissimilar nucleation site densities in samples T and P, which results in very different lateral domain sizes of the grown 2D crystals. An atomic-resolution AFM image of the $WS_2/Al_2O_3(001)$ surface depicted in Fig. 1(c) shows the hexagonal lattice arrangements of the top S and W atomic layers of one of the $WS_2$ 2D domains from sample P. The atomic resolution AFM is only partly beneficial in studying the structural details of the $WS_2/Al_2O_3(001)$ surface since the buried interface is not directly observable via this top-down method.

In-house, grazing incidence X-ray diffraction (GIXRD) measurements were performed to determine the in-plane crystallographic orientation of the $WS_2$ 2D crystals relative to the sapphire lattice. The in-plane radial GIXRD scans, depicted in Figs. 1(d, e), reveal that for sample T, the $WS_2(110)$ direction is parallel to $Al_2O_3(100)$, whereas in sample P, $WS_2(110)$ is parallel to $Al_2O_3(110)$. Therefore, the in-plane hexagonal lattices of $WS_2$ and $Al_2O_3(001)$ form domain epitaxy with $5\times a_{WS2}$ on $2\sqrt{3}\times a_{Al2O3}$ as for sample T or $3\times a_{WS2}$ on $2\times a_{Al2O3}$ as for sample P. The $WS_2$ hexagonal in-plane lattice parameter was determined to be *3.149(1) Å* and *3.151(1) Å* for samples T and P, respectively, which is contracted by ~*1.3%* compared to bulk $WS_2$. Azimuthal $\phi$-scans at fixed in-plane scattering vector $Q = 4\pi \, \mathrm{Sin}\theta/\lambda$, presented in Figs. S3(a, b) show Bragg peaks confirming the *30°* relative difference in the epitaxial registry between samples T and P. This *30°* relative change in $WS_2$ crystal orientations is partly due to having **a**-axis and **m**-axis miscut arrangements in samples T and P, respectively. However, a previous work on $MoS_2/Al_2O_3(001)$ growth has demonstrated that regardless of **a**-axis or **m**-axis substrate step edge arrangements, $MoS_2$ retains the same epitaxial registry as $MoS_2(110) \parallel Al_2O_3(100)$.[35] It has also been shown that this *R30°* epitaxy (i.e., 2D TMD nanocrystal (110) || $Al_2O_3(100)$) is energetically the most favorable in-plane lattice orientation for the $MoS_2/Al_2O_3(001)$.[35] Another report has shown that the amount of S passivation at the substrate surface can result in different orientations of $MoS_2$ 2D crystals on $Al_2O_3(001)$.[36] This was also in agreement with $WSe_2/Al_2O_3(001)$ growth work in finding that a Se passivated surface along with substrate edge step can lead to two local minima on the potential energy surface at *0°/60°* (i.e., 2D TMD crystal (100) || $Al_2O_3(100)$) and at *30°* for orienting the 2D crystal on sapphire .[37] These results suggest that the observed differences in the epitaxial registry of $WS_2/Al_2O_3(001)$ samples studied in the present work can be attributed to structurally and chemically differing interface structures in samples T and P.

Our samples possess *7-10°* of offset between the surface step direction and substrate crystal direction. However, in each case, $WS_2$ 2D crystals align along the $Al_2O_3$ crystallographic axis either following $WS_2(110) \parallel Al_2O_3(100)$ as in sample T or following $WS_2(100) \parallel Al_2O_3(100)$ as in sample P (discussed in the Supporting Information (SI)). Therefore, although the surface step edges of the substrate crystal help to eliminate the misaligned $WS_2$ domain formation during the nucleation and lateral growth process it does not fully guide the unidirectional orientation. Rather, the grown $WS_2$ crystals obey the epitaxial relationship with the substrate lattice. A similar finding was also reported for $WSe_2(001)/Al_2O_3(001)$, where it was observed that the substrate step edges do not exclusively control the $WSe_2$ 2D domain orientation, instead, the 2D domains orient themselves to the substrate lattice and can deviate the exact step edge angles by several degrees.[37] The in-plane $L = 0$ reciprocal space maps for $WS_2$ (110) $\parallel$ $Al_2O_3$ (100) and $WS_2$ (110) $\parallel$ $Al_2O_3$ (110) epitaxy configurations are displayed in Figs. S4(a, b).

We measured the scattered X-ray intensity along the 00L reciprocal space rod for out-of-plane interface structural information, as displayed in Fig. 1(f). Here, we compare the measured 00L CTRs for samples T and P with the calculated 00L CTR for a bare $Al_2O_3(001)$ surface. The difference in 00L CTR features from samples T and P indicates variation in interface structures due to differences in growth recipes. The interface models that fit these two data sets will be described below.

XP spectra used to determine the stoichiometry and chemical state of the interfacial species are shown in Figs. 2(a-d). Ideally, $WS_2$ should have two $S^{2-}$ ions for every $W^{4+}$ ion. The W 4*f* and S 2*p* core level XPS measurements show striking deviation from this ideal case. In sample T, $W^{6+}$ and $W^{4+}$ are present with a coverage ratio of $W^{4+}/W^{6+}=$ *2.3(1)*, whereas sample P only has $W^{4+}$. On the other hand, sample P has a coverage ratio of $S^{2-}/W^{4+}=$ *3.1(1)*, which is greater than that of sample T, where $S^{2-}/W^{4+}=$ *2.5(1)*. These XPS results indicate that samples T and P possess W or S interfacial species other than those in the $WS_2$ 2D crystal. The differences in the extra W or S species for samples T and P are consistent with the differences in the initial MOCVD steps for each process.

During the initial growth step of sample T, only the W precursor ($W(CO)_6$) was flowing for *5* minutes without any S source, and then a controlled flow of both W and S precursors was started to grow the $WS_2$ domains. At the growth temperature, $W(CO)_6$ reacts chemically with the atoms on the O-terminated $Al_2O_3(001)$ substrate to produce a modified surface that acts as the interface for the subsequent $WS_2$ growth. To fully understand the interface structures of $WS_2/Al_2O_3(001)$ in sample T, it is essential to probe the surface structure of $Al_2O_3(001)$ after the initial growth treatment. To examine the surface structure of $W(CO)_6$ treated $Al_2O_3(001)$, a separate sample was taken out of the MOCVD chamber before switching on the S source. W 4*f* XPS of this intermediate sample, presented in Fig. 2(e), confirms the presence of $W^{6+}$ at the surface. No S and no $W^{4+}$ were detected. We label this sample as $WO_3/Al_2O_3(001)$ since W ions should be in *6+* charge state if they form $WO_3$, which we will confirm later in the analysis.

From a W $L\alpha$ XRF measurement, as presented in Fig. 2(f), the absolute atomic coverage of the $WO_3/Al_2O_3(001)$ sample was determined to be *6.3* W/*nm*$^2$. This is compared to *5.11* Al/*nm*$^2$ in the A-site and the same areal density for Al atoms in the B-site. These two symmetry inequivalent Al sites are labeled in the ball-and-stick model of Fig. 3(e). To locate the W atomic site(s) relative to the substrate lattice for this *0.62* ML $WO_3/Al_2O_3(001)$ surface, we used the XSW excited XRF technique (discussed in SI).[21-23] Here, we measured the modulation in the W $L\alpha_1$ XRF yield while scanning through several $\boldsymbol{H} = h\ k\ l$ substrate Bragg reflections, as shown in Figs. 3(a-d). These modulations are converted into model-independent Fourier components, $F_H = f_H e^{(2\pi i P_H)}$, for the W atomic distribution, $\rho(\boldsymbol{r})$. The measured Fourier amplitudes, $f_{\boldsymbol{H}}$, and phases, $P_{\boldsymbol{H}}$, listed in Table S2, were then used in a Fourier summation[38-40]

$$\rho(r) = 1 + 2\sum_{\substack{H \neq -H \\ H \neq 0}}^{\cdot} f_H \cos\left[2\pi\left(P_H - H \bullet r\right)\right] \quad (1)$$

to produce a 3D model-independent W atomic density map relative to the $Al_2O_3$ substrate lattice shown in Fig. 3(e). For this map, we used the first two allowed reflections along the specular direction, (0 0 6) and (0 0 12), with off-specular reflections (1 0 4) and (0 1 2) and their symmetry equivalents.

The *b*-axis projection of the 3D W map superimposed on the $Al_2O_3$ bulk-like ball-stick model, as depicted in Fig. 3(f), shows that W primarily sits *0.47 Å* above the $Al_A$ site. A much smaller population of W is also present at *0.13 Å* above the $Al_B$ site, as seen from the 2D cut of the model-independent atomic density map presented in Fig. 3(e).

To better quantify these assigned lattice positions and occupancies, we use a model that assumes a fraction $c_A$ of the W atoms sits at the $\boldsymbol{r}_A = (2/3\ 1/3\ z_A)$ A-site and that $c_B$ of the W atoms sit at the $\boldsymbol{r}_B = (1/3\ 2/3\ z_B)$ B-site. The fraction of correlated W is $C = c_A + c_B$, and (1 - C) is the fraction of W uncorrelated with the substrate lattice. The $H^{th}$ Fourier component for the W distribution in this model is:

$$F_H = f_H e^{i2\pi P_H} = ¿ \overset{c}{\left(¿¿ A e^{i2\pi H.r_A} + c_B e^{i2\pi H.r_B}\right)} e^{-(Q\sigma)^2/2} \quad (2)$$

Using an isotropic Debye-Waller displacement distribution with Gaussian-width $\sigma = 0.1$ Å, we performed a least-squares global fit of this model to the four sets of XSW-XRF measured $f_H$ and $P_H$ values to find that *41(1)%* of the W atoms sit at *0.45(1) Å* above the $Al_A$ site, *14(1)*% sit at *0.30(3) Å* above the $Al_B$ site, and the remaining *45%* are uncorrelated with the $Al_2O_3$ lattice. We also checked the single $W_A$ site (or $W_B$ site) model by fixing $c_B = 0$ (or $c_A = 0$) in the XSW-XRF analysis, which showed a much worse fit (see Table S3). Therefore, both model-independent and model-dependent XSW-XRF results are consistent regarding the incorporation of $W^{6+}$ ions into the surface of $Al_2O_3$.

As our XSW-XRF method has a limited length-scale and is insensitive to surface oxygen(s), we used specular (00L) and off-specular (10L, 11L, and 20L) CTR measurements, as presented in Figs. 4(a-d). Here, the diffuse scattering streaks between the $Al_2O_3$ Bragg peaks in reciprocal space are sensitive to the surface atomic rearrangement.[2, 41] However, unlike the XSW method, the structure factor phase information is lost in the measured CTR intensities, and a direct transformation of scattering data into electron density is not possible. To solve this issue, we used a modified Fienup algorithm[42], which links the measured 00L CTR reflectivity and the unmeasured phases by iteratively adjusting the phase of the structure factor. This direct-method analysis generates a model-independent 1D electron density profile for the extended interfacial structure with sub-*Å* resolution under the constraints that the substrate structure is known, and the unknown electron density inside the interfacial region is positive and goes to zero above the interfacial region. We used the XSW-XRF-derived W distribution as the starting condition. The model-independent analysis of the 00L CTR data and the generated 1D electron density profile are shown in Figs. 4(a, e), respectively. From this analysis, we find that above the $Al_A$ site, there is an electron density peak (marked as 1 in Fig. 4(e)) at a height *0.48(2) Å* above the bulk-like $Al_A$ site. We have identified this atomic layer as $W^{6+}$, along with small contributions from B-site $Al^{3+}$ and B-site $W^{6+}$ ions. In addition, we observed two more electron density peaks (labeled as 2 and 3) above layer 1 W (and Al) ions. The Z locations and occupancies of different atomic layers are listed in Table 1. Peak 2 is assigned as surface hydroxyl oxygens bound to $W^{6+}$, and peak 3 is attributed to the oxygens of physically adsorbed surface water molecules. Similar findings have been reported for a hydrated $\alpha$-$Al_2O_3$ (001) surface studied using CTR scattering and theory calculations.[41, 43] Since X-rays primarily scatter from electrons, CTR data is insensitive to H species in the 1D electron density map. The formation of layer 2 oxygens (hydroxylated) on top of layer 1 W/Al can be explained by considering the dangling bonds of W/Al cations, which are prone to react with O anions. We will analyze the off-specular CTR to find the lateral coordinates of these surface oxygens. Similar findings have been reported for a hydrated $\alpha$-$Al_2O_3$ (001) surface studied using CTR scattering and theory calculations.[41, 43] Since X-rays primarily scatter from electrons, CTR data is insensitive to H species in the 1D electron density map. The formation of layer 2 oxygens (hydroxylated) on top of layer 1 W/Al can be explained by considering the dangling bonds of W/Al cations, which are prone to react with O anions. To find the lateral coordinates of these surface oxygens, we will analyze the off-specular CTR.

The Fienup-based model-independent analysis helps to avoid ambiguities arising from model assumption, specifically when the structure is unknown. After determining the 1D projection of the structure from Fienup, a complete model-based 3D analysis of CTR data is necessary to achieve a more complete result. A model-dependent simultaneous fit of specular and off-specular CTR data sets was performed using a Python-based program, GenX.[44] Here, we compare the calculated structure factor for a given model with the measured CTR and refine the structural parameters to meet convergence criteria. In GenX, the optimization of parameters is conducted through the differential evolution method (a generic algorithm), which helps to avoid any local minima when finding a converged solution. The model-dependent best fits for the $WO_3/Al_2O_3(001)$ CTR data are presented in Figs. 4(a-d), and the *b*-axis projection of the refined 3D model is depicted in Fig. 4(f). The GenX-determined atomic occupancies and xyz coordinates are listed in Table S4. From this analysis, we determine that the $W^{6+}$ ions occupy *40(2) %* of the $Al_A$ sites at a height of *0.47(1) Å* above that bulk-like position and *10(3)%* of $Al_B$ sites at a height of *0.26(1) Å* above that bulk-like position. Al ions partially occupy the remaining A and B sites at the surface. The off-specular CTR simulated for a hypothetical case of $W^{6+}$ ions occupying *10%* of the $Al_A$ sites and *40%* of $Al_B$ sites shows a much worse match with the measured profile, as depicted in Fig. S9(b). Several test simulations that confirm the presence of oxygen atoms in layer 2 above the W/Al ions and show how sensitive the CTR data is for a change in the position of those oxygens are presented in Fig. S9. This confirms the formation of $WO_3$ as a result of $W^{6+}$ incorporation in the $Al_2O_3(001)$ surface during the MOCVD process. A cross-sectional side view along $Al_2O_3(110)$ direction of the near-surface atoms in the $WO_3/Al_2O_3(001)$ sample has been imaged using high-angle annular dark-field (HAADF)-STEM as depicted in Fig. S11(a), which agrees very well with the X-ray studies we have discussed so far. Therefore, the combined XPS, XSW-XRF, and CTR methods unambiguously determine the 3D structure of the sub-ML $WO_3$/ $Al_2O_3(001)$ system with sub-*Å* resolution.

To compare the experimentally derived atomic structure of $WO_3$/ $Al_2O_3(001)$ to theory, DFT calculations were performed. We introduced *37.5 %* site fraction W substitutions at the outermost metal bilayers of O-terminated alumina supercell structure having a mirror symmetry plane through its center (discussed in the Methods section). To allow every ion in its favored valence state, we added H atoms to the outermost oxygens of the slab as needed. The atoms in these configurations were then allowed to displace to their optimal positions according to DFT while keeping the supercell dimension fixed. The DFT-optimized atomic positions for the W and surface O ions for the *37.5%* W occupancy at $Al_A$ lateral sites agree very well with the combined X-ray results, and the corresponding atomic structure is depicted in Fig. 4(g). A side-by-side comparison of the experimental findings and DFT calculation for W-incorporated $Al_2O_3$ structure is presented in Table 1 and Fig. S12(c). The DFT calculated surface energy for the *37.5%* W occupancy at $Al_A$ lateral sites was determined to be *6.2* $\mathit{meV/Å^2}$ higher than that of the $Al_B$ case. When considering the slight difference in surface energy between the configurations with W atoms at $Al_A$ and $Al_B$ sites, one has to bear in mind that the PBE formalism we used for DFT calculations is much more precise for predicting the bond distances (the error is typically *1%* in excess of the experimental result), than predicting energies (the error is of around *10* to *20%*). In addition, there is the possibility that entropic or kinetic effects are responsible for the sign of the small difference in energy between W occupying the $Al_A$ lateral sites (as seen in the experiment) and occupying the $Al_B$ lateral sites (as given by the DFT-PBE predictions). We also tested *12.5*, *25* and *50 %* W substitutions at the outermost Al bilayer models using DFT-PBE, and according to these calculations, this energy difference is smallest when *37.5%* of the surface Al atoms are substituted by W atoms, which agrees very well with the results from the experimental characterization.

The results discussed above now set the stage for determining the extended interface structure that includes the 2D $WS_2$ and supporting $Al_2O_3(001)$ modified surface for sample T. From a combined W $L\alpha_1$ XRF (*8.4* W / $nm^2$) and W 4*f* XPS ($W^{4+}$/ $W^{6+}$= *2.3(1)*) analysis, we determine that the absolute coverage of $WS_2$ in sample T is *0.67* ML (*5.9* $W^{4+}$/ $nm^2$) and $WO_3$ coverage is *0.24* ML (*2.5* $W^{6+}$/ $nm^2$). The derived $f_H$ and $P_H$ values from the W $L\alpha_1$ XSW-XRF measurements of the $WS_2/Al_2O_3(001)$ sample T (Fig. 5(a) and Fig. S7) are listed in Table S2. With an additional W atomic position along the out-of-plane z-direction, we performed a least-squares global fit to the measured $f_H$ and $P_H$ values from the specular (0 0 6) and (0 0 12) XSW-XRF measurements with a 3-height W model (two sites for $W^{6+}$ ions in $WO_3$ interface and one site for $W^{4+}$ ions in $WS_2$). From this model-dependent analysis, we found that (i) the $WS_2/Al_2O_3(001)$ sample T possesses interfacial W structurally similar to the previously described $WO_3/Al_2O_3(001)$ sample. That is, $W^{6+}$ ions are at *0.45 Å* above the $Al_A$ sites. (ii) Unlike $WO_3/Al_2O_3(001)$, there are $W^{4+}$ ions in the 2D $WS_2$ crystal of sample T; (iii) the vertical separation between the interfacial A-site $W^{6+}$ layer and the 2D crystal $W^{4+}$ ionic layer is *5.64(2) Å* with *2.4(1)* times more $W^{4+}$ ions compared to the $W^{6+}$ interface ions. The atomic ratio between $W^{4+}$ in $WS_2$ to $W^{6+}$ in $WO_3$ obtained from XSW-XRF is consistent with the XPS result. We also performed S $K\alpha$ XSW-XRF measurements for the specular (0 0 6) and (0 0 12) reflections (Figs. S7(d, e)), to determine the S atomic positions in the $WS_2$ 2D crystal along the out-of-plane z-direction. Obtained $f_H$ and $P_H$ values from these S $K\alpha$ XSW-XRF data, as listed in Table S2, were used in a least-squares global fit to find that *38(9) %* of $S^{2-}$ ions are at *4.26(5) Å* and *43(9) %* of $S^{2-}$ ions are at *7.28(5) Å* above the origin that bisects the bulk like Al bilayer in $Al_2O_3$. The remaining *19%* $S^{2-}$ ions are uncorrelated with the $Al_2O_3$ lattice. Assuming $W^{4+}$ is located halfway in between two $S^{2-}$ ions in $WS_2$ 2D crystal along the z-direction, the $W^{4+}$ should be at *5.8(1) Å* above the Al bilayer origin. This $W^{4+}$ height corroborates very well with the W $L\alpha_1$ XSW-XRF analysis, which determines the $W^{4+}$ location as *5.84(2) Å* above the Al bilayer origin. From this analysis, the atomic ratio between $S^{2-}$ to $W^{4+}$ is found to be *2.7(6)*, which is well consistent with the XPS result ($S^{2-}/W^{4+}$= *2.5(1)*). On the other hand, the specular (006) XSW-XRF result for the $WS_2$/ $Al_2O_3(001)$ sample P (Fig. 5(b)) shows an entirely different modulation in the W $L\alpha_1$ yield, leading to a different W Fourier phase ($P_{006}$) value (see Table S2) compared to that of sample T. For $WS_2$/ $Al_2O_3(001)$ sample P, there is a single height W atomic site at *6.43(2) Å* above the center of the topmost bulk-like Al-bilayer.

The top view of the ball-and-stick models for the two different epitaxial orientations of the $WS_2$ crystals with respect to the $Al_2O_3(001)$ substrate is depicted in Fig. 5(c). To examine their extended interface structures with more detail, we measured the 00L CTR. The high X-ray photon flux ($3.0\times10^{11}$ photons per second) and low background contribution of DESY P08 facility enabled us to measure the 00L CTR up to $Q_{max}$ ~ $9$ $Å^{-1}$ for sample T, as presented in Fig. 1(f). The repeatability of measured data (Fig. S10(a)) confirms no significant X-ray radiation damage to sample T. Whereas, during the measurements of sample P, we observed that under the undulator X-ray beam, there was a noticeable change in 00L CTR features within a time frame of a *1 h* scan. We primarily attribute this much higher rate of X-ray damage to the much smaller size of the 2D crystals for sample P compared to sample T. The smaller the size, the greater the fraction of atoms at the 2D crystal edges, where the under-coordinated atoms should react more readily with the environment. To overcome this issue, we used a less intense rotating anode X-ray source ($3.3\times10^{7}$ photons per second) to measure the 00L CTR for sample P. A few consecutive scans showed reproducibility (Fig. S10(b)) to confirm the stability of sample P under this less intense X-ray beam. However, due to the drop-off in counting statistics, this limited our scan range to $Q_{max}$ ~ $6$ $Å^{-1}$, as shown in Fig. 1(f). Consequently, we have less resolution in defining the atomic locations compared to the analysis for sample T. As seen in the AFM images, both $WS_2/Al_2O_3(001)$ samples possess surface lateral inhomogeneities due to the non-coalesced triangular 2D domains. Unlike $WO_3$/ $Al_2O_3(001)$, we need to consider scattering from the portion of the surface covered by $WS_2$ separate from the remaining portion not covered by $WS_2$. Specifically, when the size of the $WS_2$ domains is larger than the projected X-ray coherence footprint, it is necessary to add the scattering contributions from the two different types of surfaces incoherently, as in the case for $WS_2/Al_2O_3(001)$ sample T, but not for sample P. To analyze the data for sample T, we calculated the structure factor as described in Eqs. (S3-S5) and incoherently added the scattered intensities from the two different surfaces to simulate the CTR intensity. For sample P, we used a coherent sum of the complex scattering amplitudes (Eqs. (S8-S10)). The structural parameters for the $WS_2/Al_2O_3(001)$ systems were optimized to get the best match of calculated CTR with measured 00L data, as presented in Fig. 1(f). The best-fit 1D electron density profiles for the surface atomic layers in samples T and P are shown in Fig. 5(d). The *Å* coordinates and occupation fractions for the atomic layers in these extended interface structures are listed in Table 2.

This model-dependent 00L CTR analysis is consistent with our XSW-XRF findings for the starting $WO_3$/ $Al_2O_3(001)$ surface, as it shows an interfacial $WO_3$ seed layer between $WS_2$ and $Al_2O_3(001)$ with the $WO_3$ $W^{6+}$ ions at *0.48(3) Å* above the bulk-like $Al_A$ site. The 00L CTR is also consistent with $H_2O$ molecules physisorbed to the portion of the surface which is not covered by the $WS_2$ 2D crystals. The CTR determined that the vertical separation between the interfacial $W^{6+}$ and $WS_2$ $W^{4+}$ is *5.49(3) Å*, which is only *0.15 Å* smaller than that measured by XSW. A cross-sectional HAADF-STEM imaging measures the same vertical separation between $W^{4+}$ and $W^{6+}$ ions as ~ *6 Å*, as presented in Fig. S11(b). However, this STEM derived separation is not unambiguous and possesses different values ranging between *5-10 Å* depending on the different local areas and specimens cut out from the same sample under study. This is expected, given the highly localized analysis of the STEM technique and possible specimen damage to the delicate Q-vdW epilayer system during preparation and by the high-energy electron irradiation during imaging, compared to the relatively non-destructive X-ray measurements of this buried interface structure. The CTR analysis also independently corroborates our XPS results in finding *2.2(1)* times more $W^{4+}$ in the $WS_2$ than $W^{6+}$ at the $WO_3$ interface. A schematic side view of the extended interface structure derived from our combined X-ray analysis for the sample T is depicted in Fig. 5(e).

For sample P, the model-dependent 00L CTR interface analysis is consistent with having an AlS termination to the $Al_2O_3(001)$ substrate with the $W^{4+}$ ions in the $WS_2$ layer *6.50(4) Å* above the origin of our coordinate system which bisects the bulk like Al bilayer at the surface. Compared to the previously discussed XSW-XRF determined value, this only differs by *0.07 Å*. The CTR determined coverage ratio between total S and $W^{4+}$ is *3.2(1)*, which is consistent with the findings of the previously discussed XRF and XPS measurements. To compare the experimental results for the interface structure of sample P with theory, DFT calculations were performed. As presented in Table 2, the DFT calculated atomic Z coordinates for the surface structure of sample P agree very well with the combined X-ray analysis. A schematic side view of the extended interface structure of sample P derived from the DFT optimization is depicted in Fig. 5(e). We also calculate the adhesion energy for the $WS_2$ crystal on the AlS terminated $\alpha$-$Al_2O_3$ to be *25 meV/Å²*, which falls in the typical range of adhesion energies for layered vdW materials.[45] In comparison, the adhesion energy for the $WS_2$ on the $WO_3$ terminated $\alpha$-$Al_2O_3$ slab was found to be *54 meV/Å²*.[17] This points to a stronger vdW bonding of the $WS_2$ to the $WO_3$ terminated surface than to the AlS terminated surface. This also agrees with our XSW and CTR finding that the $WS_2$ in sample T has a smaller vdW gap at the interface than that in sample P.

Therefore, the present work demonstrates how two different pre-growth treatments lead to $W^{6+}$ or $S^{2-}$ incorporation in the $Al_2O_3(001)$ substrate surface resulting in $WO_3$ or AlS interfaces for the subsequent epitaxial growth of sub-ML $WS_2$ 2D crystals. These chemically and structurally dissimilar interfaces cause different vdW gaps between the grown $WS_2$ crystals and $Al_2O_3(001)$ substrate crystals. Eventually, this changes the vdW interaction at the 2D crystal-substrate interfaces, which could be the reason for the significant differences in the nucleation density and hence the lateral domain sizes of the grown $WS_2$ 2D crystals. Due to the change in lateral domain sizes, the $WS_2$ crystals process different structural stability. These findings should be useful for optimizing the device grade preparation of 2D $WS_2$ semiconductors. Realizing a low-power TMD FET device requires integrating an ML TMD material with metallic gates and ultrathin high-*k* dielectrics in through-plane geometry. However, sapphire, being an insulator, cannot serve as a back gate, making it difficult to form the FET device. That's why most TMD FET devices reported in literature are usually made by exfoliating and transferring the TMD layer onto a back-gated dielectric substrate. This has several limitations, including loss of structural integrity of the exfoliated TMD layer, introduction of contaminates during transfer, and small-area processing. In contrast, low-power operating TMD FET can also be fabricated by growing ML 2D TMD directly on a thin $Al_2O_3$ dielectric layer grown by atomic layer deposition (ALD) on Si substrate, as demonstrated in a previous work on $MoS_2$.[46] Further studies are needed to explore different interface-induced FET performances in prototype $WS_2/Al_2O_3$ systems.

## CONCLUSIONS:

In our work, different MOCVD conditions were used for growing $WS_2/Al_2O_3(001)$ samples T and P, resulting in dissimilar chemical and atomic structures at the interfaces between the supported 2D nanocrystals and substrate. During the growth of $WS_2/Al_2O_3(001)$ sample T, the $O_2$ annealing of $Al_2O_3(001)$ substrate leads to O-termination, which reacts with $W(CO)_6$ at growth temperature and produces a $WO_3$ incorporated $Al_2O_3(001)$ surface. This $WO_3$ terminated $Al_2O_3(001)$ surface acts as a seed layer for growing the 2D $WS_2$ crystals. On the other hand, for the growth of sample P, due to $H_2$ annealing of $Al_2O_3(001)$ at high temperature, the substrate possesses an Al-terminated surface. Due to dangling bonds, the Al-termination is ionically unstable and reacts immediately with the $H_2S$ gas precursor during the initial growth stage and forms an AlS terminal surface layer. The S atomic layer forms the interface between the $WS_2$ 2D nanocrystal and the underlying $Al_2O_3(001)$ substrate crystal. A combination of relatively non-destructive X-ray techniques, namely XSW-XRF and CTR, in conjunction with XPS is used to unambiguously probe the element-specific atomic resolution structures of these extended interfaces. Our experimental findings are in agreement with our DFT structural models. The observed differences in the $WS_2$ lateral domain sizes, epitaxial registry, and different vdW gaps are related to the differing interfaces in samples T and P. These findings should be very informative for further developing device-grade 2D TMD sample growth applicable to FET devices.

**Supporting Information:** details of experimental setups, X-ray measurements, $Al_2O_3(001)$ substrate miscut, $WS_2$ in-plane orientation, chemical state, XSW analysis, CTR simulation, HAADF-STEM interface cross-section, DFT calculated energies, and interface structure.

## ACKNOWLEDGMENTS:

This work was supported by DOE/BES Award No. DE-SC0023450 to the Hydrogen in Energy and Information Sciences EFRC at Northwestern University (NU). D.G. was supported by DOE contract no. DEAC02-07CH11359 to the Superconducting Quantum Materials and Systems Center. The 5ID-C DNDCAT beamline at the Advanced Photon Source (APS) was used for XSW measurements. The APS, an Office of Science User Facility operated for DOE by Argonne National Laboratory, is supported by DOE under Contract DE-AC0206CH11357. The P08 beamline at PETRA III Deutsches Elektronen-Synchrotron (DESY), a member of the Helmholtz Association HGF, was used for CTR measurements. This work also made use of the XRD, and Keck-II XPS facilities at NU supported by the MRSEC program (NSF DMR-2308691), Keck Foundation, State of Illinois, and the Soft and Hybrid Nanotechnology Experimental (SHyNE) Resource (NSF ECCS-2025633). Sample T was grown at Tel Aviv University, N.S., and A.I. acknowledge the generous support from the Israel Science Foundation, grant # 2596/21. Sample P was grown in the 2D Crystal Consortium Materials Innovation Platform (2DCC-MIP) facility at Penn State, which is supported by the National Science Foundation (NSF) under NSF cooperative agreement NSF DMR-2039351. S.M. and M.B. thank Paul Fenter (Argonne National Lab), Joanne Stubbs (University of Chicago), and Peter Eng (University of Chicago) for helpful discussions on CTR data analysis. R.A. acknowledges funding from the Spanish MICIU (PID2023-151080NB-I00/AEI/10.13039/501100011033 and CEX2023-001286-S MICIU/AEI / 10.13039/501100011033) and by the MICIU with funding from European Union Next Generation EU (PRTR-C17.I1) promoted by the Government of Aragon (DGA) as well from the DGA project E13-23R. The STEM studies have been conducted at the Laboratorio de Microscopias Avanzadas (LMA), Universidad de Zaragoza.

## REFERENCES:

(1) Cao, Y.; Fatemi, V.; Fang, S.; Watanabe, K.; Taniguchi, T.; Kaxiras, E.; Jarillo-Herrero, P. Unconventional Superconductivity in Magic-Angle Graphene Superlattices. *Nature* **2018**, *556* (7699), 43-50. DOI: https://doi.org/10.1038/nature26160.

(2) Emery, J. D.; Detlefs, B.; Karmel, H. J.; Nyakiti, L. O.; Gaskill, D. K.; Hersam, M. C.; Zegenhagen, J.; Bedzyk, M. J. Chemically Resolved Interface Structure of Epitaxial Graphene on SiC(0001). *Phys. Rev. Lett.* **2013**, *111* (21), 215501. DOI: 10.1103/PhysRevLett.111.215501.

(3) Liu, X. L.; Hersam, M. C. Interface Characterization and Control of 2D Materials and Heterostructures. *Adv. Mater.* **2018**, *30* (39). DOI: https://doi.org/10.1002/adma.201801586.

(4) Pierucci, D.; Mahmoudi, A.; Silly, M.; Bisti, F.; Oehler, F.; Patriarche, G.; Bonell, F.; Marty, A.; Vergnaud, C.; Jamet, M.; Boukari, H.; Lhuillier, E.; Pala, M.; Ouerghi, A. Evidence for Highly p-Type Doping and Type II Band Alignment in Large Scale Monolayer $WSe_2$/Se-Terminated GaAs Heterojunction Grown by Molecular Beam Epitaxy. *Nanoscale* **2022**, *14* (15), 5859-5868. DOI: http://dx.doi.org/10.1039/D2NR00458E.

(5) Manzeli, S.; Ovchinnikov, D.; Pasquier, D.; Yazyev, O. V.; Kis, A. 2D Transition Metal Dichalcogenides. *Nat. Rev. Mater.* **2017**, *2* (8). DOI: https://doi.org/10.1038/natrevmats.2017.33.

(6) Chaves, A.; Azadani, J. G.; Alsalman, H.; da Costa, D. R.; Frisenda, R.; Chaves, A. J.; Song, S. H.; Kim, Y. D.; He, D. W.; Zhou, J. D.; Castellanos-Gomez, A.; Peeters, F. M.; Liu, Z.; Hinkle, C. L.; Oh, S. H.; Ye, P. D.; Koester, S. J.; Lee, Y. H.; Avouris, P.; Wang, X. R.; Low, T. Bandgap Engineering of Two-Dimensional Semiconductor Materials. *npj 2D Mater. Appl.* **2020**, *4* (1). DOI: https://doi.org/10.1038/s41699-020-00162-4.

(7) Choi, W.; Choudhary, N.; Han, G. H.; Park, J.; Akinwande, D.; Lee, Y. H. Recent Development of Two-Dimensional Transition Metal Dichalcogenides and Their Applications. *Mater. Today* **2017**, *20* (3), 116-130. DOI: 10.1016/j.mattod.2016.10.002.

(8) Wang, Q. H.; Kalantar-Zadeh, K.; Kis, A.; Coleman, J. N.; Strano, M. S. Electronics and Optoelectronics of Two-Dimensional Transition Metal Dichalcogenides. *Nat. Nanotechnol.* **2012**, *7* (11), 699-712. DOI: 10.1038/Nnano.2012.193.

(9) Sebastian, A.; Pendurthi, R.; Choudhury, T. H.; Redwing, J. M.; Das, S. Benchmarking Monolayer $MoS_2$ and $WS_2$ Field-Effect Transistors. *Nat. Commun.* **2021**, *12* (1). DOI: https://doi.org/10.1038/s41467-020-20732-w.

(10) Fan, Y.; Zhou, Y. Q.; Wang, X. C.; Tan, H. J.; Rong, Y. M.; Warner, J. H. Photoinduced Schottky Barrier Lowering in 2D Monolayer $WS_2$ Photodetectors. *Adv. Opt. Mater.* **2016**, *4* (10), 1573-1581. DOI: https://doi.org/10.1002/adom.201600221.

(11) Sheng, Y. W.; Chen, T. X.; Lu, Y.; Chang, R. J.; Sinha, S.; Warner, J. H. High-Performance $WS_2$ Monolayer Light-Emitting Tunneling Devices Using 2D Materials Grown by Chemical Vapor Deposition. *Acs Nano* **2019**, *13* (4), 4530-4537. DOI: http://dx.doi.org/10.1021/acsnano.9b00211.

(12) Leem, Y. C.; Fang, Z. Y.; Lee, Y. K.; Kim, N. Y.; Kakekhani, A.; Liu, W. J.; Cho, S. P.; Kim, C.; Wang, Y. H.; Ji, Z. R.; Patra, A.; Kronik, L.; Rappe, A. M.; Yim, S. Y.; Agarwal, R. Optically Triggered Emergent Mesostructures in Monolayer $WS_2$. *Nano Lett.* **2024**, *24* (18), 5436-5443. DOI: 10.1021/acs.nanolett.4c00358.

(13) Xie, L.; Wang, L.; Liu, X.; Chen, J.; Wen, X.; Zhao, W.; Liu, S.; Zhao, Q. Flexible Tungsten Disulfide Superstructure Engineering for Efficient Alkaline Hydrogen Evolution in Anion Exchange Membrane Water Electrolysers. *Nat. Commun.* **2024**, *15* (1), 5702. DOI: 10.1038/s41467-024-50117-2.

(14) Li, K. L.; Wang, W. J. Effects of Substrates on the Optical Properties of Monolayer $WS_2$. *J. Cryst. Growth* **2020**, *540*. DOI: https://doi.org/10.1016/j.jcrysgro.2020.125645.

(15) Su, L. Q.; Yu, Y. F.; Cao, L. Y.; Zhang, Y. Effects of Substrate Type and Material-Substrate Bonding on High-Temperature Behavior of Monolayer $WS_2$. *Nano Res.* **2015**, *8* (8), 2686-2697. DOI: https://doi.org/10.1007/s12274-015-0775-1.

(16) Maslen, E. N.; Streltsov, V. A.; Streltsova, N. R.; Ishizawa, N.; Satow, Y. Synchrotron X-ray Study of the Electron Density in $\alpha$-$Al_2O_3$. *Acta Crystallogr., Sect. B: Struct. Sci.* **1993**, *49*, 973-980. DOI: 10.1107/S0108768193006901.

(17) Cohen, A.; Mohapatra, P. K.; Hettler, S.; Patsha, A.; Narayanachari, K. V. L. V.; Shekhter, P.; Cavin, J.; Rondinelli, J. M.; Bedzyk, M.; Dieguez, O.; Arenal, R.; Ismach, A. Tungsten Oxide Mediated Quasi-van der Waals Epitaxy of $WS_2$ on Sapphire. *Acs Nano* **2023**, *17* (6), 5399-5411. DOI: 10.1021/acsnano.2c09754.

(18) Eichfeld, S. M.; Hossain, L.; Lin, Y.-C.; Piasecki, A. F.; Kupp, B.; Birdwell, A. G.; Burke, R. A.; Lu, N.; Peng, X.; Li, J.; Azcatl, A.; McDonnell, S.; Wallace, R. M.; Kim, M. J.; Mayer, T. S.; Redwing, J. M.; Robinson, J. A. Highly Scalable, Atomically Thin $WSe_2$ Grown via Metal-Organic Chemical Vapor Deposition. *Acs Nano* **2015**, *9* (2), 2080-2087. DOI: 10.1021/nn5073286.

(19) Chubarov, M.; Choudhury, T. H.; Hickey, D. R.; Bachu, S.; Zhang, T. Y.; Sebastian, A.; Bansal, A.; Zhu, H. Y.; Trainor, N.; Das, S.; Terrones, M.; Alem, N.; Redwing, J. M. Wafer-Scale Epitaxial Growth of Unidirectional $WS_2$ Monolayers on Sapphire. *Acs Nano* **2021**, *15* (2), 2532-2541. DOI: 10.1021/acsnano.0c06750.

(20) Dosch, H.; Batterman, B. W.; Wack, D. C. Depth-Controlled Grazing-Incidence Diffraction of Synchrotron X Radiation. *Phys. Rev. Lett.* **1986**, *56* (11), 1144-1147. DOI: DOI 10.1103/PhysRevLett.56.1144.

(21) Bedzyk, M. J.; Cheng, L. W. X-ray Standing Wave Studies of Minerals and Mineral Surfaces: Principles and Applications. *Rev Mineral Geochem* **2002**, *49* (Applications of Synchrotron Radiation in Low-Temperature Geochemistry and Environmental Sciences), 221-266. DOI: https://doi.org/10.2138/gsrmg.49.1.221.

(22) Woodruff, D. P. Surface Structure Determination using X-ray Standing Waves: a Simple View. *Rep. Prog. Phys.* **2005**, *68*, 743-798. DOI: https://doi.org/10.1088/0953-8984/6/49/007.

(23) Zegenhagen, J. Surface Structure Determination with X-ray Standing Waves. *Surf. Sci. Rep.* **1993**, *49*, 202-271. DOI: https://doi.org/10.1016/0167-5729(93)90025-K.

(24) Robinson, I. K.; Tweet, D. J. Surface X-ray Diffraction. *Rep. Prog. Phys.* **1992**, *55* (5), 599-651. DOI: 10.1088/0034-4885/55/5/002.

(25) Andrews, S. R.; Cowley, R. A. Scattering of X-rays from Crystal Surfaces. *J. Phys. C: Solid State Phys.* **1985**, *18* (35), 6427-6439. DOI: Doi 10.1088/0022-3719/18/35/008.

(26) Robinson, I. K. Crystal Truncation Rods and Surface-Roughness. *Phys. Rev. B* **1986**, *33* (6), 3830-3836. DOI: https://doi.org/10.1103/PhysRevB.33.3830.

(27) Cohen, A.; Patsha, A.; Mohapatra, P. K.; Kazes, M.; Ranganathan, K.; Houben, L.; Oron, D.; Ismach, A. Growth-Etch Metal−Organic Chemical VaporDeposition Approach of $WS_2$ Atomic Layers. *Acs Nano* **2021**, *15* (1), 526-538. DOI: 10.1021/acsnano.0c05394.

(28) Walko, D. A.; Sakata, O.; Lyman, P. F.; Lee, T. L.; Tinkham, B. P.; Okasinski, J. S.; Zhang, Z.; Bedzyk, M. J. Surface And Interface Studies At APS Endstation 5ID-C. *Synchrotron Radiat. Instrum.* **2004**, *705*, 1166-1169. DOI: https://doi.org/10.1063/1.1758007.

(29) Seeck, O. H.; Deiter, C.; Pflaum, K.; Bertam, F.; Beerlink, A.; Franz, H.; Horbach, J.; Schulte-Schrepping, H.; Murphy, B. M.; Greve, M.; Magnussen, O. The High-Resolution Diffraction Beamline P08 at PETRA III. *J. Synchrotron Radiat.* **2012**, *19*, 30-38. DOI: 10.1107/S0909049511047236.

(30) Schlepütz, C. M.; Herger, R.; Willmott, P. R.; Patterson, B. D.; Bunk, O.; Brönnimann, C.; Henrich, B.; Hülsen, G.; Eikenberry, E. F. Improved Data Acquisition in Grazing-Incidence X-ray Scattering Experiments using a Pixel Detector. *Acta Crystallogr. A Found. Adv.* **2005**, *61*, 418-425. DOI: 10.1107/S0108767305014790.

(31) Kresse, G.; Furthmuller, J. Efficient Iterative Schemes for Ab Initio Total-Energy Calculations using a Plane-Wave Basis Set. *Phys. Rev. B* **1996**, *54* (16), 11169-11186. DOI: DOI 10.1103/PhysRevB.54.11169.

(32) Kresse, G.; Furthmuller, J. Efficiency of Ab-Initio Total Energy Calculations for Metals and Semiconductors using a Plane-Wave Basis Set. *Comput. Mater. Sci.* **1996**, *6* (1), 15-50. DOI: Doi 10.1016/0927-0256(96)00008-0.

(33) Perdew, J. P.; Burke, K.; Ernzerhof, M. Generalized Gradient Approximation Made Simple. *Phys. Rev. Lett.* **1997**, *78* (7), 1396-1396. DOI: https://link.aps.org/doi/10.1103/PhysRevLett.77.3865.

(34) Monkhorst, H. J.; Pack, J. D. Special Points for Brillouin-Zone Integrations. *Phys. Rev. B* **1976**, *13* (12), 5188-5192. DOI: DOI 10.1103/PhysRevB.13.5188.

(35) Li, T. T.; Guo, W.; Ma, L.; Li, W. S.; Yu, Z. H.; Han, Z.; Gao, S.; Liu, L.; Fan, D. X.; Wang, Z. X.; Yang, Y.; Lin, W. Y.; Luo, Z. Z.; Chen, X. Q.; Dai, N. X.; Tu, X. C.; Pan, D. F.; Yao, Y. G.; Wang, P.; Nie, Y. F.; Wang, J. L.; Shi, Y.; Wang, X. R. Epitaxial Growth of Wafer-Scale Molybdenum Disulfide Semiconductor Single Crystals on Sapphire. *Nat. Nanotechnol.* **2021**, *16* (11), 1201-1207. DOI: https://doi.org/10.1038/s41565-021-00963-8.

(36) Suenaga, K.; Ji, H. G.; Lin, Y. C.; Vincent, T.; Maruyama, M.; Aji, A. S.; Shiratsuchi, Y.; Ding, D.; Kawahara, K.; Okada, S.; Panchal, V.; Kazakova, O.; Hibino, H.; Suenaga, K.; Ago, H. Surface-Mediated Aligned Growth of Monolayer $MoS_2$ and In-Plane Heterostructures with Graphene on Sapphire. *Acs Nano* **2018**, *12* (10), 10032-10044. DOI: 10.1021/acsnano.8b04612.

(37) Zhu, H. Y.; Nayir, N.; Choudhury, T. H.; Bansal, A.; Huet, B.; Zhang, K. Y.; Puretzky, A. A.; Bachu, S.; York, K.; Mc Knight, T. V.; Trainor, N.; Oberoi, A.; Wang, K.; Das, S.; Makin, R. A.; Durbin, S. M.; Huang, S. X.; Alem, N.; Crespi, V. H.; van Duin, A. C. T.; Redwing, J. M. Step Engineering for Nucleation and Domain Orientation Control in $WSe_2$ Epitaxy on c-Plane Sapphire. *Nat. Nanotechnol.* **2023**, *18* (11), 1295-+. DOI: 10.1038/s41565-023-01456-6.

(38) Bedzyk, M. J.; Fenter, P. XSW Imaging. In *The X-Ray Standing Wave Technique: Principles and Applications*, Zegenhagen, J., Kazimirov, A. Eds.; World Scientific, 2013; pp 289-302.

(39) Cheng, L.; Fenter, P.; Bedzyk, M. J.; Sturchio, N. C. Fourier-Expansion Solution of Atom Distributions in a Crystal Using X-Ray Standing Waves. *Phys. Rev. Lett.* **2003**, *90*, 255503. DOI: https://doi.org/10.1103/PhysRevLett.90.255503.

(40) Feng, Z. X.; Kim, C. Y.; Elam, J. W.; Ma, Q.; Zhang, Z.; Bedzyk, M. J. Direct Atomic-Scale Observation of Redox-Induced Cation Dynamics in an Oxide-Supported Monolayer Catalyst: $WO_x/\alpha\text{-}Fe_2O_3(0001)$. *J. Am. Chem. Soc.* **2009**, *131* (51), 18200-+. DOI: 10.1021/ja906816y.

(41) Eng, P. J.; Trainor, T. P.; Brown, G. E.; Waychunas, G. A.; Newville, M.; Sutton, S. R.; Rivers, M. L. Structure of The Hydrated $\alpha\text{-}Al_2O_3$ (0001) Surface. *Science* **2000**, *288* (5468), 1029-1033. DOI: 10.1126/science.288.5468.1029.

(42) Fenter, P.; Zhang, Z. Model-Independent One-Dimensional Imaging of Interfacial Structures at <1Å Resolution. *Phys. Rev. B* **2005**, *72* (8). DOI: https://doi.org/10.1103/PhysRevB.72.081401.

(43) Hass, K. C.; Schneider, W. F.; Curioni, A.; Andreoni, W. The Chemistry of Water on Alumina Surfaces: Reaction Dynamics from First Principles. *Science* **1998**, *282* (5390), 882-882. DOI: 10.1126/science.282.5387.265.

(44) Glavic, A.; Björck, M. GenX 3: The Latest Generation of an Established Tool. *J. Appl. Crystallogr.* **2022**, *55*, 1063-1071. DOI: 10.1107/S1600576722006653.

(45) Rokni, H.; Lu, W. Direct Measurements of Interfacial Adhesion in 2D Materials and van der Waals Heterostructures in Ambient Air. *Nat. Commun.* **2020**, *11* (1). DOI: https://doi.org/10.1038/s41467-020-19411-7.
(46) Bergeron, H.; Sangwan, V. K.; McMorrow, J. J.; Campbell, G. P.; Balla, I.; Liu, X. L.; Bedzyk, M. J.; Marks, T. J.; Hersam, M. C. Chemical Vapor Deposition of Monolayer $MoS_2$ Directly on Ultrathin $Al_2O_3$ for Lowpower Electronics. *Appl. Phys. Lett.* **2017**, *110* (5). DOI: http://dx.doi.org/10.1063/1.4975064.

## TOC

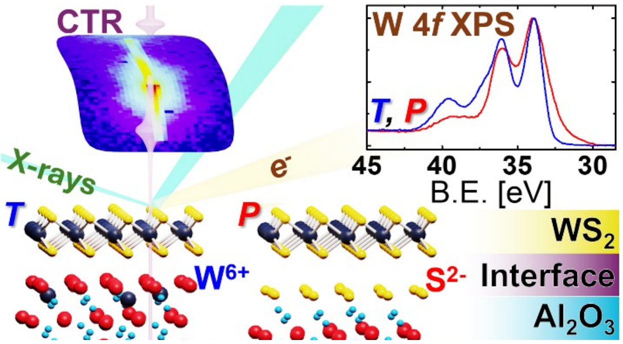

## Figures

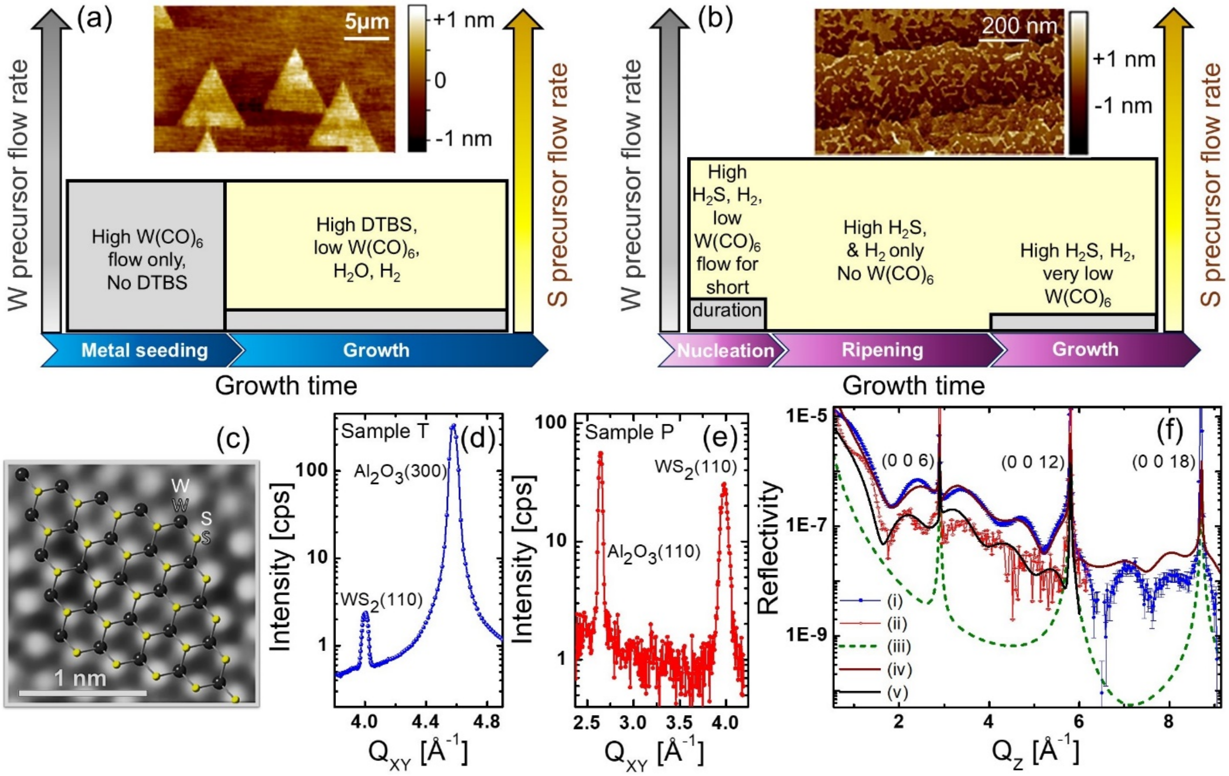

**Figure 1.** Schematic diagrams of the multistep synthesis processes for the $WS_2/Al_2O_3(001)$ (a) sample T and (b) sample P sub-monolayer growth. Insets show AFM images of the $WS_2/Al_2O_3(001)$ surfaces for (a) sample T, and (b) sample P, showing differences in lateral domain sizes of the 2D crystals. (c) Atomic-resolution AFM image depicting hexagonal lattice arrangements of the top S and W atomic layers of a $WS_2$ 2D crystal from sample P. (d, e) GIXRD radial scans showing in-plane Bragg peaks from $WS_2$/ $Al_2O_3(001)$ samples T and P, respectively. (f) Specular CTR data for $WS_2$/ $Al_2O_3(001)$ (i) sample T, (ii) sample P, along with calculated profiles for (iii) bulk-like $Al_2O_3(001)$ substrate, and structural models for (iv) sample T and (v) sample P.

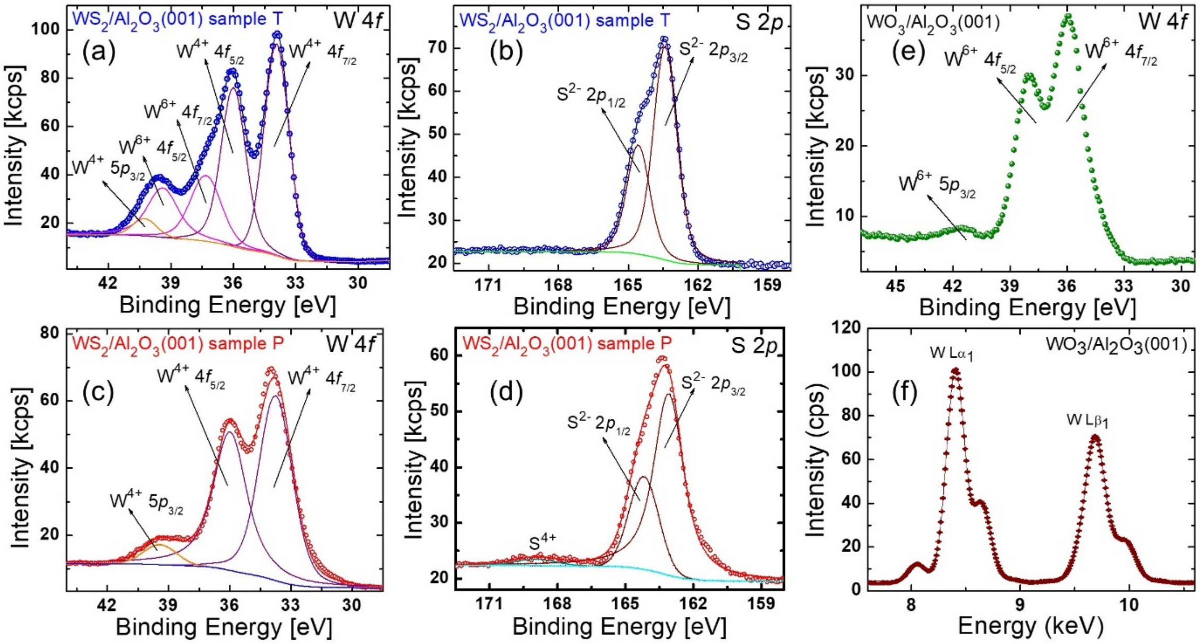

**Figure 2.** XP spectra of W 4f and S 2p doublets for $WS_2$/ $Al_2O_3(001)$ (a, b) sample T and (c, d) sample P. (e) W 4f XPS for $WO_3$/ $Al_2O_3(001)$ sample. (f) The W L XRF spectrum from the $WO_3$/ $Al_2O_3(001)$ sample.

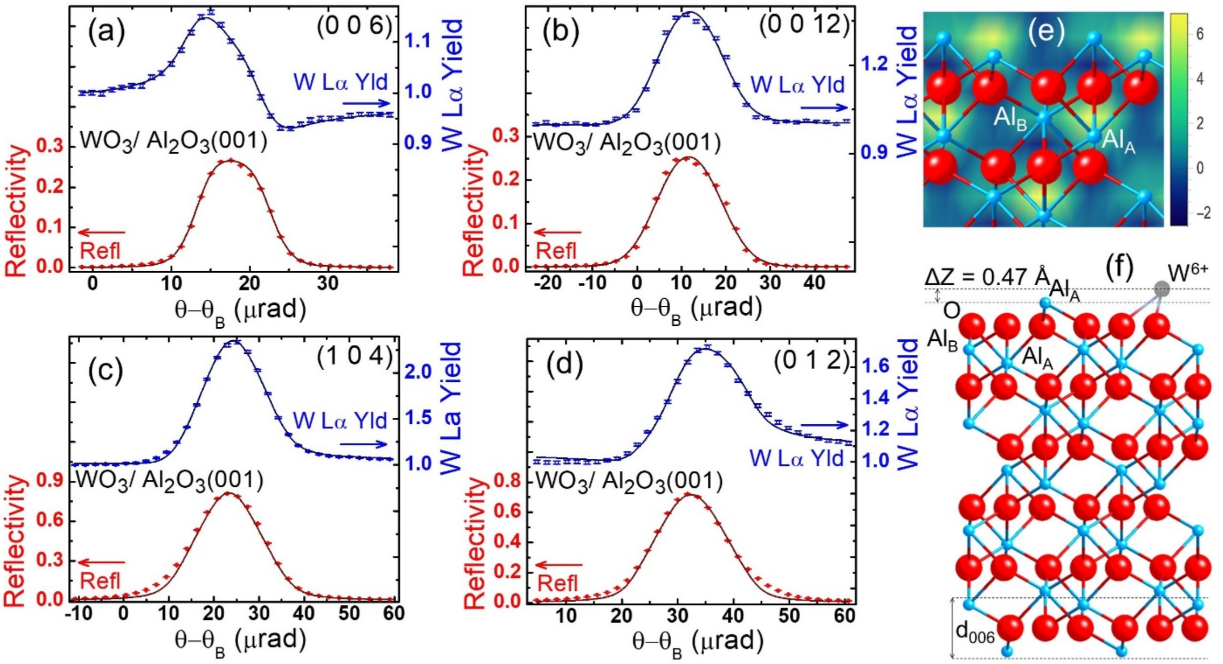

**Figure 3.** $WO_3$/ $Al_2O_3$(001) XSW-XRF analysis: (a-d) reflectivity and W Lα yield data and best fits for angle θ scans through the (0 0 6), (0 0 12), (1 0 4), and (0 1 2) Bragg peaks. (e) $Al_2O_3$ model superimposed on a (110) planar cut through the maxima in the model-independent W 3D density map generated by the XSW-XRF measurements. (f) $W^{6+}$ position with respect to the *b*-axis projection of $Al_2O_3$(001) ball-and-stick model.

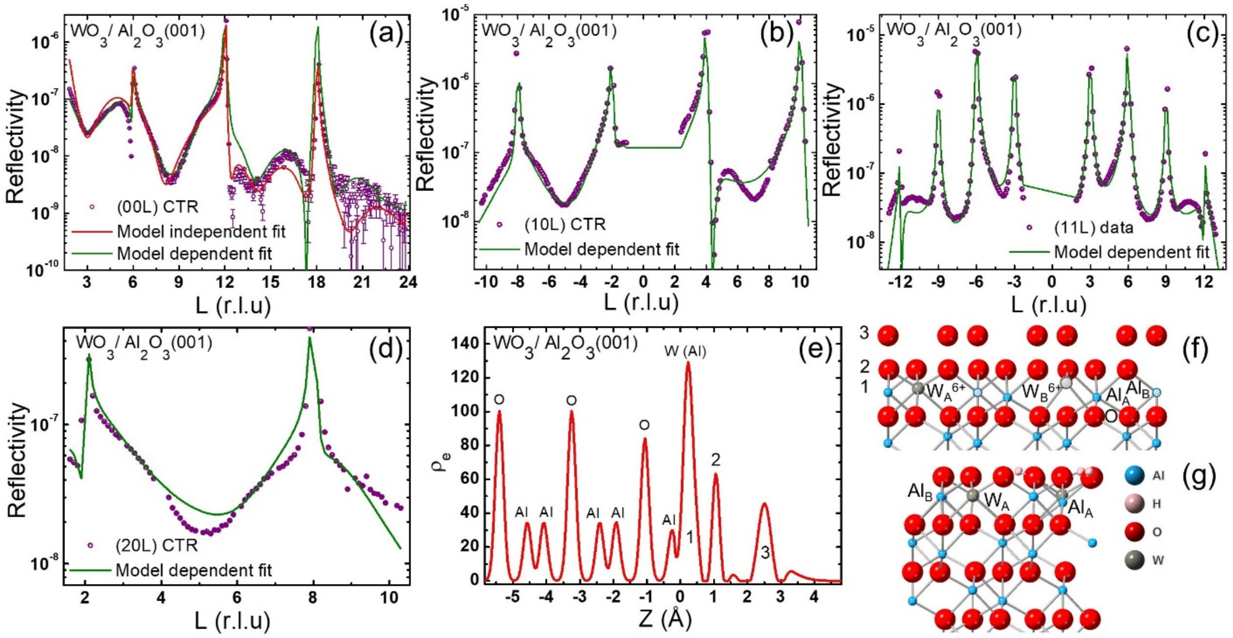

**Figure 4.** For the $WO_3$/ $Al_2O_3$(001) sample, (a-d) specular and off-specular CTR data along with best fits. (e) 1D electron density profile from model-independent 00L CTR analysis. The locations and occupancies of the electron density peaks labeled 1-3 are listed in Table 1. *b*-axis projection of the (f) 3D structure obtained from model-dependent refinement of specular and off-specular CTR data sets, (g) DFT optimized $Al_2O_3$ symmetric supercell slab structure with W incorporated at the outermost $Al_A$ lateral sites and H atom adsorbed at the outermost O sites.

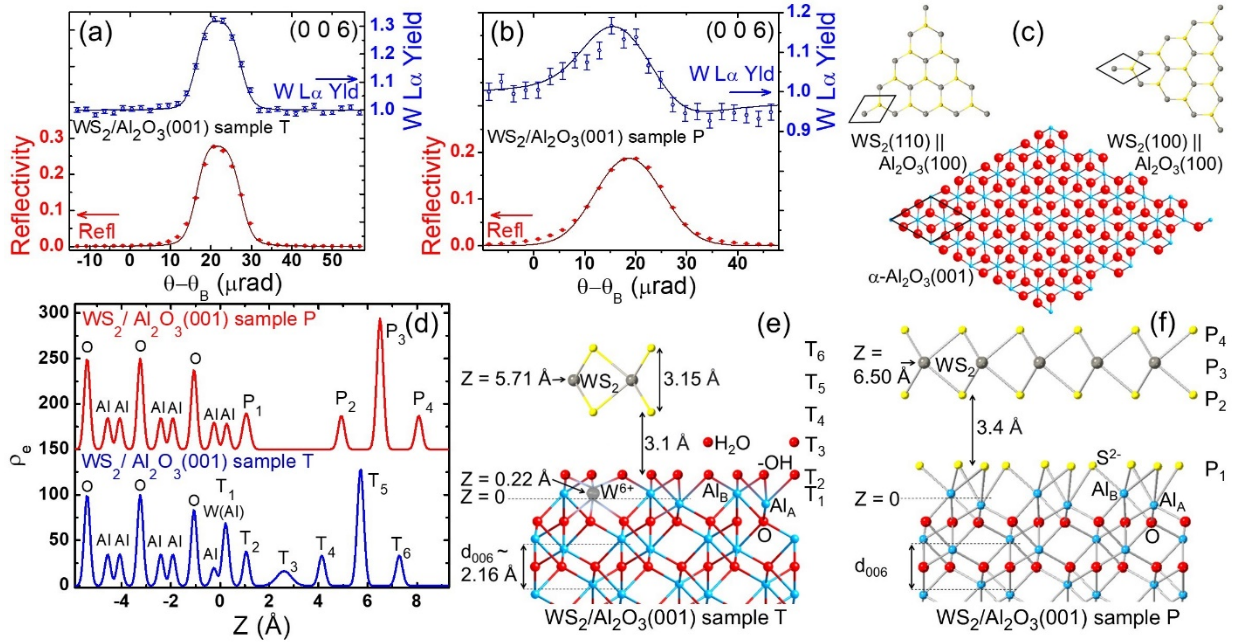

**Figure 5.** For the $WS_2$/ $Al_2O_3(001)$ samples: (a, b) XSW-XRF reflectivity, W Lα yield data and best fits for (a) sample T and (b) sample P. (c) Top views of ball-and-stick models for $Al_2O_3(001)$ substrate and $WS_2$ 2D crystals with GIXRD determined orientations for sample T shown on the left and sample P on the right. (d) 1D electron density profiles for $WS_2$/ $Al_2O_3(001)$ near-surface atomic layers for samples T and P derived from model-dependent 00L CTR analysis shown in Fig. 1(f). For clarity, the profile for sample P has been shifted vertically. The locations and occupancies of the electron density peaks labeled $T_{1\text{-}6}$ and $P_{1\text{-}4}$ are listed in Table 2. *b*-axis projection of the models for (e) sample T determined by combined X-ray analysis, and (f) sample P obtained from DFT analysis. The horizontal dashed lines mark the bulk-like (006) planes, which bisect the bulk-like $Al_A$ and $Al_B$ sites.

**Table 1.** Z coordinates (with respect to the origin bisecting the bulk like Al bilayer at the surface) and occupancies of the surface atoms in $WO_3/Al_2O_3(001)$ structure obtained from 00L CTR 1D electron density profile analysis and DFT optimization. For the DFT calculation, we introduced 37.5 *%* site fraction of W substitutions at the outermost $Al_A$ sites in the O-terminated $Al_2O_3$ supercell.

| **Model-independent CTR analysis** | | | | **DFT optimization** |
|---|---|---|---|---|
| Atom | e / atomic layer | Occupancy | Position (*Å*) | Avg. position (*Å*) |
| **O of adsorbed $H_2O$ Peak 3** | *20.46* | *2.05* | *2.50* | |
| O of -OH Peak 2 | *16.12* | *1.61* | *1.06* | *1.03* |
| **$W^{6+}$ ($Al_B^{3+}$) Peak 1** | *49.88* | *0.64* | *0.24* | *0.27 (0.21)* |
| **$Al_A^{3+}$** | *6.92* | *0.69* | *-0.27* | *-0.05* |
| **$O^{2-}$** | *25.17* | *2.52* | *-1.06* | *-1.08* |
| **$Al_B^{3+}$** | *10* | *1* | *-1.92* | *-1.91* |
| **$Al_A^{3+}$** | *10* | *1* | *-2.41* | *-2.41* |
| **$O^{2-}$** | *30* | *3* | *-3.25* | *-3.24* |
| **$Al_B^{3+}$** | *10* | *1* | *-4.08* | *-4.08* |
| **$Al_A^{3+}$** | *10* | *1* | *-4.57* | *-4.57* |
| **$O^{2-}$** | *30* | *3* | *-5.40* | *-5.40* |

**Table 2.** Z coordinates (with respect to the origin bisecting the bulk like Al bilayer at the surface) and occupancies of the surface atoms in $WS_2/Al_2O_3(001)$ sample T and sample P obtained from 00L CTR 1D electron density profile analysis and DFT calculation for sample P.

| **CTR $WS_2/Al_2O_3(001)$ sample T** | | | **CTR $WS_2/Al_2O_3(001)$ sample P** | | | **DFT sample P** |
|---|---|---|---|---|---|---|
| Atom | Occupancy | Position (Å) | Atom | Occupancy | Position (Å) | Avg. position (Å) |
| **$S^{2-}$ Peak $T_6$** | *0.61* | *7.28* | | | | |
| **$W^{4+}$ Peak $T_5$** | *0.61* | *5.71* | $S^{2-}$ Peak $P_4$ | *0.68* | *8.07* | *8.14* |
| **$S^{2-}$ Peak $T_4$** | *0.61* | *4.13* | $W^{4+}$ Peak $P_3$ | *0.68* | *6.50* | *6.58* |
| **O of adsorbed $H_2O$ Peak $T_3$** | *1.20* | *2.59* | $S^{2-}$ Peak $P_2$ | *0.68* | *4.93* | *5.03* |
| O of -OH Peak $T_2$ | *1.14* | *1.06* | $S^{2}$ interface Peak $P_1$ | *0.81* | *1.06* | *1.63* |
| **$W^{6+}$ ($Al_B{}^{3+}$) Peak $T_1$** | *0.28* | *0.22* | $Al_B{}^{3+}$ | *0.82* | *0.27* | *0.29* |
| **$Al_A{}^{3+}$** | *0.57* | *-0.25* | $Al_A{}^{3+}$ | *0.86* | *-0.25* | *-0.27* |
| **$O^{2-}$** | *2.52* | *-1.06* | $O^{2-}$ | *2.64* | *-1.06* | *-1.08* |
| **$Al_B{}^{3+}$** | *1* | *-1.92* | $Al_B{}^{3+}$ | *1* | *-1.92* | *-1.91* |
| **$Al_A{}^{3+}$** | *1* | *-2.41* | $Al_A{}^{3+}$ | *1* | *-2.41* | *-2.41* |
| **$O^{2-}$** | *3* | *-3.25* | $O^{2-}$ | *3* | *-3.25* | *-3.25* |